Research

Author for correspondence:
Hermes Gadêlha
e-mail: hermes.gadelha@york.ac.uk

The counterbend dynamics of cross-linked filament bundles and flagella

Rachel Coy[1] and Hermes Gadêlha[2]

[1]CoMPLEX, University College London, London WC1E 6BT, UK
[2]Department of Mathematics, University of York, York YO10 5DD, UK

HG, 0000-0001-8053-9249

Cross-linked filament bundles, such as in cilia and flagella, are ubiquitous in biology. They are considered in textbooks as simple filaments with larger stiffness. Recent observations of flagellar counterbend, however, show that induction of curvature in one section of a passive flagellum instigates a compensatory counter-curvature elsewhere, exposing the intricate role of the diminutive cross-linking proteins at large scales. We show that this effect, a material property of the cross-linking mechanics, modifies the bundle dynamics and induces a bimodal $L^2 - L^3$ length-dependent material response that departs from the Euler–Bernoulli theory. Hence, the use of simpler theories to analyse experiments can result in paradoxical interpretations. Remarkably, the counterbend dynamics instigates counter-waves in opposition to driven oscillations in distant parts of the bundle, with potential impact on the regulation of flagellar bending waves. These results have a range of physical and biological applications, including the empirical disentanglement of material quantities via counterbend dynamics.

1. Introduction

The spontaneous generation of harmonic bending waves along a sperm flagellum has been a source of fascination since it was reported on in the late seventeenth century [1]. It was not until 1968, however, that the fundamental mechanism behind the flagellar wave propagation was unveiled [2–4]. ATP-induced inter-microtubule tangential motion is converted into transversal forces that are capable of bending the flagellar assembly altogether, laying the empirical basis for the sliding filament theory for eukaryotic flagellum.

Notably, almost one decade before the discovery of the interfilament sliding [2,3,5], the existence of such active elements along the sperm flagellum was theorized via a simple fluid–structure interaction model [6]. Machin demonstrated that the combined action of viscous and elastic dissipation experienced by a slender filament rapidly damps any driven oscillation along its length, thus requiring the action of contractile elements in order to sustain large waving amplitude [7]. Later, Wiggins & Goldstein [8] elegantly demonstrated that the elastohydrodynamics of any simple Euler–Bernoulli filament moving in a viscous fluid leads to a hyperdiffusive dissipation of bending, characterized by a bending penetration length ℓ_ω, which can be further exploited to extract material parameters from biological filaments in a wide range of length scales [9]. Hitherto, the elastohydrodynamics of active and passive filaments have generated a vast literature of analytical, computational and empirical studies across disciplines [10–19].

Despite the inherent complexity of filament bundles [20–31], as exemplified by the axonemal flagellum [23,24], with its $9 + 2$ cross-linked microtubule doublets arranged in a cylindrical fashion [23], the textbook elastic bending stiffness has been estimated using a simplistic linear relation between bending moment and curvature [27–31], as derived from Euler–Bernoulli rod theory [32]. Incidentally, the inadequacy of classical rod theories, from Euler–Bernoulli to Timoshenko–Cosserat [32], emerged via paradoxical counterbend empirical responses, figure 1a, first observed by Lindemann and colleagues [33,37], and
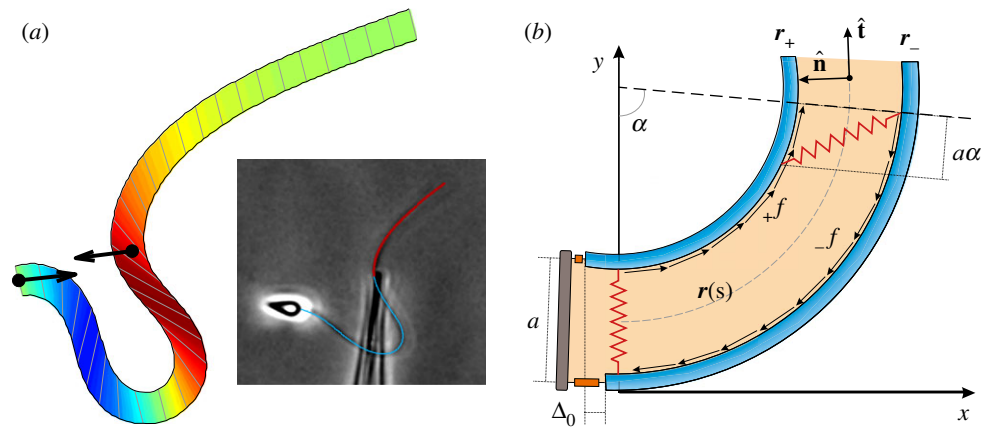
Figure 1. The counterbend phenomenon and geometry of deformation: (*a*) Micrograph showing the static configuration of a sea urchin sperm rendered passive with its head attached to the coverslip while forced externally by a microprobe [33], together with the geometrically exact filament-bundle model prediction. Red curve shows the model curve fitting result from Gadêlha *et al.* [34]. (*b*) Two-dimensional representation of the axoneme and the sliding filament mechanism with basal compliance [7,34–36]. Micrograph adapted from Gadêlha *et al.* [34]. (Online version in colour.)

later captured via a geometrically exact mechanical model by Gadêlha *et al.* [34] (figure 1*a*). These studies revealed how the induction of curvature in one section of a passive sperm flagellum instigates compensatory counter-curvature elsewhere, namely the counterbend phenomenon [33,37]. They established the critical role of the diminutive elastic linking-proteins while instigating large-amplitude deformations, inherently coupling distant parts along the bundle assembly, despite their small slenderness ratio [33,34,37]. More recently, the counterbend phenomenon was also exploited in order to extract material quantities from *Chlamydomonas* flagella [38], despite the relatively short-length flagella. The dynamical response of the counterbend phenomenon in passive cross-linked bundles still remains unexplored in the literature.

The discovery of the counterbend phenomenon highlighted the current need to reassess both the established material measurements [20–22,25–31,35] and the resulting mechanical response, from statics to dynamics, of cross-linked filament bundles [27–31]. The former is crucial in a broad range of biological structures, from the cytoskeleton of eukaryotic cells to cellular division, cross-bridge muscle contraction and locomotion, via structures like the axoneme. A fundamental challenge, both experimentally and theoretically, is, therefore, to understand how this complex structure yields bulk material properties and overall cellular mechanical responses and, ultimately, function. In active bundles, the consequences of using inadequate material parameters, which have been used for the past 30 years to investigate flagellar waves [7,11,38–49], are still unknown. This is further confronted with an increasing number of, repeatedly contradicting, active control models for the flagellar wave coordination [7,11,36,40,41,44,45,47–52]. Paradoxically, in order to induce bending waves, flagellar control models rely on the implementation of filament-bundle deformations, in distinct material directions, that are yet to be scrutinized in isolation, from curvature [39,41,46,49] to inter-filament sliding [7,11,36,45,52,53], and axial distortions [44,47,50]. This is aggravated by the strong coupling between the unknown activity, and the passive and dissipative components, leading to the non-identifiability of parameters when contrasted against experiments [54,55]. Without the disentanglement between the passive and active elements, and without the rationalization of the resultant mechanical response of cross-linked filament bundles, it is unclear, for

example, which competing flagellar control hypothesis [7,11,36,40,41,44,45,47–51], if any, is able to provide a quantitative understanding of the flagellar regulation and, crucially, function of the internal mechanics and structure. Indeed, any comprehensive model of flagellar bending self-organization depends on reliable measurements of mechanical and material properties of the system in the absence of activity [34,38].

Here, we complement the seminal work by Machin [6] and Wiggins & Goldstein [8] on the dynamics of passive filaments, and demonstrate how the nanometric cross-linking proteins that are present in passive cross-linked filament bundles instigate novel dynamical counterbend phenomena. This is in contrast with previous models on flagellar wave coordination [7,11,36,40,41,44,45,47–52], which incorporate the cross-linking interaction in conjunction with molecular motor dynamics. We consider the dynamical situation in which only the structural passive elements are present. For axonemal filament bundles, this corresponds to the empirical situation in which molecular motors are rendered passive [33,37,38]; figure 1*a*. The filament-bundle elastohydrodynamical model unveils the occurrence of counter-travelling waves in distant parts of bundle, reducing the propulsive potential of driven oscillations, and even reversing the propulsive direction, from pushing to pulling hydrodynamics. We show that the interplay between the interfilament sliding at the base and cross-linking dissipation elsewhere gives rise to a bimodal $L^2 - L^3$ length-dependent material response that departs from canonical Euler–Bernoulli theory. Hence, the use of simpler rod theories to analyse experiments can result in paradoxical interpretations. Furthermore, the counterbend dynamics offers a robust way to measure material quantities empirically, bypassing cumbersome force-displacement experiments at the microscale [30,31,33,37,38]; figure 1*a*. These results further suggest that the dynamical counter-wave phenomena is likely to play a critical role on the waveform organization, and the subsequent wave direction, of long flagella [48,49,56].

2. Cross-linked filament-bundle elastohydrodynamics

We consider a planar representation of cross-linked filament bundles and flagellar axonemes, as depicted in figure 1*b*,

used interchangeably hereafter, composed of two elastic, inextensible filaments that resist deformation with an elastic bending modulus E [7,34–36]. Each constituent filament $\mathbf{r}_{\pm}(s, t) = \mathbf{r}(s, t) \pm a/2\hat{\mathbf{n}}(s, t)$ is separated by a distance a, much smaller than the filament length $a \ll L$, normal to the centre line $\mathbf{r}(s, t)$ at every point in arclength s and time t. Geometry constrains the normal vector $\hat{\mathbf{n}}(s, t) = -\sin\alpha\mathbf{e}_x + \cos\alpha\mathbf{e}_y$ to the plane, where α is the angle between the fixed frame x-axis and the tangent to the centre line $\hat{\mathbf{t}} = \mathbf{r}_s$. Like a rail-track [35], the constituent filaments travel distinct contour lengths forcing a geometrical arclength mismatch $\Delta(s, t) = \Delta_0(t) + a(\alpha(s, t) - \alpha_0(t))$, where Δ_0 and α_0 are the length mismatch and tangent angle at $s = 0$ (figure 1b). Points of equal contour length along the filament bundle are connected by elastic links which generate a shearing force, and thus an internal moment, proportional to the sliding displacement $f(s, t) = k\Delta(s, t)$ with an elastic sliding resistance k. At the basal end, the additional connecting compliance across the filaments, commonly found in spermatozoa and inhomogeneous bundles, is Hookean $\kappa_e\Delta_0(t) = -\int_0^L f(s', t)\,\mathrm{d}s'$ with a spring constant κ_e [34,36] (figure 1b).

For asymptotically slender filament bundles, the hydrodynamic forces experienced by an infinitesimal element is anisotropic and linearly related to the local velocity $\mathbf{f}_{\mathrm{vis}} = -\zeta_\perp(\hat{\mathbf{n}}.\mathbf{r}_t)\hat{\mathbf{n}} - \zeta_\parallel(\hat{\mathbf{t}}.\mathbf{r}_t)\hat{\mathbf{t}}$, where $\zeta_\perp$, $\zeta_\parallel$ are the lowest order resistive coefficients derived from inertialess hydrodynamics [27,28]. Contact forces are not defined constitutively due to the inextensibility constraint [32]. The filament-bundle elastohydrodynamics is governed by the balance of contact forces and contact moments

$$-E\alpha_{ssss} + a^2k\alpha_{ss} = \zeta_\perp\alpha_t, \qquad (2.1)$$

simplified here for small curvatures [8,9,11,36]. The filament-bundle shape is given by the initial value problem $\mathbf{r}(s, t) = \mathbf{r}(0, t) + \int_0^s (\cos\alpha(s', t), \sin\alpha(s', t))\,\mathrm{d}s'$ for an arclength s and time t. Boundary conditions ensure the total balance of forces, $F(s) = -E\alpha_{ss} + af(s, t)$, and torques, $M(s) = -E\alpha_s + a\int_s^L f(s', t)\,\mathrm{d}s'$, acting on the bundle [32,34], as detailed in the electronic supplementary material, S1. The resulting cross-linking mechanics couples distant parts along the bundle via the total momentum balance, now modified non-locally by

$$f(s, t) = -\frac{k^2a}{kL + \kappa_e}\int_0^L (\alpha(s') - \alpha_0)\,\mathrm{d}s' + ka(\alpha(s) - \alpha_0)$$

(the electronic supplementary material, S1). Dissipation from different material directions are mediated by the hydrodynamic drag. The filament-bundle dynamics is dictated by the interplay between the elastohydrodynamic hyperdiffusion [8,9] and the cross-linking diffusion [7,35,36]. These boundary moments alter the hyperdiffusion balance in equation (2.1) and instigate novel long-range phenomena as we explore below.

2.1. The counterbend dynamics: angular actuation

The post-transient behaviour of the shape dynamics is captured by single frequency solutions of the form $\alpha(s, t) = \mathrm{Re}\{\tilde{\alpha}(s)\,e^{-i\omega t}\}$. After convenient rescaling, the eigenvalue problem reduces to $r^4 - \mu r^2 - i\,Sp^4 = 0$, with eigenfunctions $\alpha(s, t) = \mathrm{Re}\{\sum_{j=1}^4 C_j\,e^{r_js - it}\}$, where the coefficients C_j are determined by non-local boundary moments (the electronic supplementary material, S1). The dimensionless filament-bundle compliance parameter, also referred to as sperm number, $Sp = L(\zeta_\perp\omega/E)^{1/4}$, captures the battle

between elastic and viscous forces [8], while the sliding resistance parameter, $\mu = a^2L^2k/E$, compares bending stiffness with the cross-linking resistance [34,36]. The basal compliance is given by $\gamma = kL/(kL + \kappa_e)$, and varies from $\gamma = 0$, corresponding to no interfilament sliding at the base, to $\gamma = 1$, for free basal sliding [34,36].

The emergence of the non-local, counterbend dynamics is depicted in figure 2 for a sinusoidal angular actuation of the proximal end (electronic supplementary material, Movie S1) with $\mathbf{r}_t(0, t) = 0$, and zero force and torque condition at the distal end (the electronic supplementary material, S1). An angular amplitude of 0.4362 rad is used to limit the maximum radius of curvature to 0.1. Figure 2 contrasts Machin's original solutions, figure 2a,b, with the filament-bundle post-transient dynamics, figure 2c,d. Travelling waves originating from the distal end, indicative of the non-local counterbend effect [34], can be clearly seen in figure 2c,d. A relatively small sliding displacement Δ (overlaid colour in figure 2c,d), equivalent to only half of the bundle diameter, is capable of deforming the bundle non-locally with the same magnitude of the imposed actuation.

The amplitude modulation $A(s)$, phase $\Phi(s)$ and velocity of propagation $v_p(s) = 1/\partial_s\Phi$ are depicted in figure 3, following suitable transformation to solutions of the form $\alpha(s, t) = A(s)\cos(t - \Phi(s))$. The abrupt change in wave direction is triggered by the loss in monotonicity of the phase. Non-local counter-waves propagate in the opposite direction from the distal end with a non-uniform decaying magnitude along the arclength due to the high-order dissipation. This is in contrast with the one-directional wave propagation of Euler–Bernoulli filaments, $\mu = 0$ in figure 3. The sharp change in wave direction coincides with reduced wave amplitudes at this point in arclength (figure 3). Interestingly, the non-local actuation of cross-linking moments at distal parts of the bundle is delayed by the overdamped dynamics, as indicated by the proximal–distal phase difference. Higher Sp causes larger proximal–distal phase mismatch, faster decay of the counterbend wave speed and amplitude, indicative of a destructive interference between proximal and distal waves in figures 2d and 3b, demonstrated by the sharp jump in phase in figure 3.

The counterbend dynamics impacts significantly the resulting hydrodynamic propulsion. The time-averaged propulsive force $\bar{F}_x$ exerted by fluid on the filament bundle is obtained by integrating the x component of the local drag force, $\mathbf{f}_{\mathrm{vis}} = -\zeta_\perp(\hat{\mathbf{n}}.\mathbf{r}_t)\hat{\mathbf{n}} - \zeta_\parallel(\hat{\mathbf{t}}.\mathbf{r}_t)\hat{\mathbf{t}}$, along the length of the bundle and averaging over one period of oscillation [8,9,14,15,57], as detailed in the electronic supplementary material, S1. Owing to the symmetry of the oscillations around the x-axis, the y component of the propulsive force averages to zero. Following [8,15], we conveniently rescale length by $(E/\omega\zeta_\perp)^{1/4}$ and time by $2\pi/\omega$, so that the averaged propulsive force in the x-direction may be written as

$$\bar{F}_x = \frac{\omega\zeta_\perp}{2\pi}\sqrt{\frac{E}{\omega\zeta_\perp}}\,Y_x(Sp, \mu, \gamma)$$

with a common elastohydrodynamic factor multiplying the force scaling function $Y_x(Sp, \mu, \gamma)$, which is now modified by the cross-linking mechanics. The force scaling function $Y_x(Sp, \mu, \gamma)$ depicted in figure 4 captures the comparative propulsive potential between different points in the parameter space (Sp, μ, γ), where $-\bar{F}_x$ is the force exerted by the fluid on the filament bundle [8,15,57]. For a simple Euler–Bernoulli
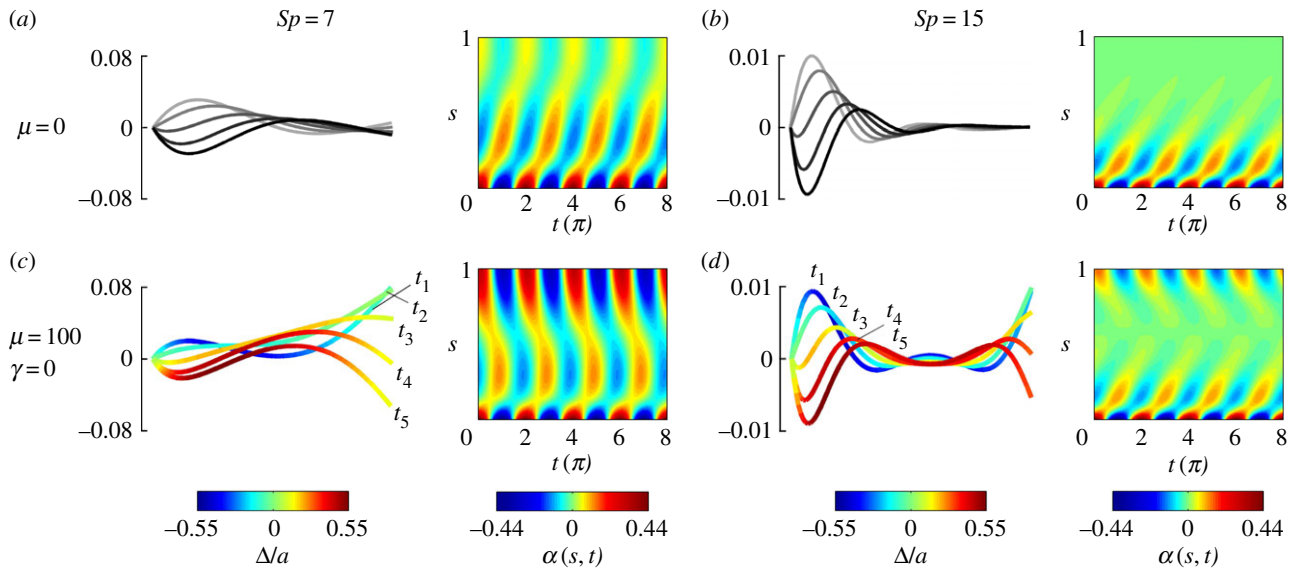
Figure 2. Counter travelling wave formation in filament bundles. (a,b) Euler–Bernoulli hyperdiffusive waveforms and (c,d) filament-bundle waveforms for $\gamma = 0$, $\mu = 100$. The rescaled sliding displacement Δ/a is overlaid in the waveform in (c,d). The time progression of the waveforms runs from t_1 to t_5, covering one-half of the periodic solution. For the α plots, the time is labelled in multiples of π. (Online version in colour.)
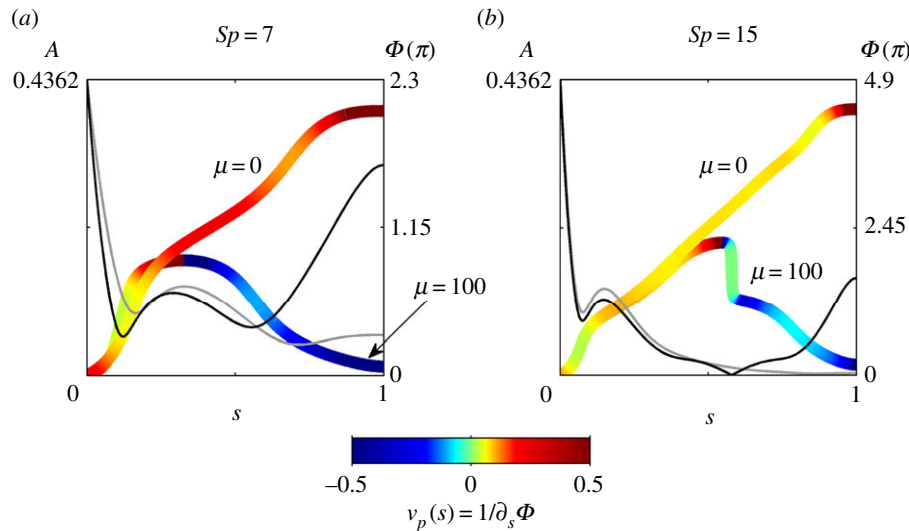

Figure 3. The amplitude A of the solutions in the $\mu = 0$ and $\mu = 100$ cases are represented by the grey and black lines, respectively; the amplitude of the coloured lines indicates the values of Φ at each point along the flagella as a multiple of π, with the colour denoting the velocity. Note that all velocities below -0.5 and above 0.5 are coloured the same as each of these values, respectively. For all of the cases featured in the plot, $\gamma = 0$. (Online version in colour.)

filament ($\mu = 0$), dashed curve in figure 4, the propulsive force is always positive, except for effectively stiff filaments ($Sp = 0$), in which no propulsion can be generated $Y_x = 0$ [8,15,58]. This is in accordance with Purcell's scallop theorem, where no net propulsion can be achieved via time-reversible motion in inertialess fluids [8,15,58]. As Sp increases, the filament becomes effectively more flexible, breaking Purcell's scallop theorem, thus inducing an increasingly large hydrodynamic propulsion, characterized by the emergence of a maximum value (dashed curve in figure 4). Increased filament floppiness, large Sp, causes the hydrodynamic force to decay and plateau. In this limit, the main contribution of the propulsive force arises from the tangential component of the hydrodynamic drag. Floppy filaments are unable to induce sizeable deformations, causing the filament to move effectively back and forth tangentially, along its length in the x direction. The

sweet spot of the hydrodynamic propulsion depicted in figure 4 (dashed curve) is the signature of the competition between viscous drag and bending stiffness, captured by the so-called penetration length $\ell_\omega = (E/\omega\zeta_\perp)^{1/4}$ [8,9,15]; first predicted by Wiggins & Goldstein [8] and empirically observed by Yu *et al.* [15].

A very distinct scenario is observed for filament bundles. As the basal compliance becomes stiffer, by reducing γ, the cross-linking mechanics switch from a mostly local contribution with small counterbend deformations ($\gamma = 1$ in figure 4), to non-local effects, with increasingly large amplitudes at the distal end ($\gamma = 0$ in figure 4, inset). Ultimately, this causes the propulsive force to vanish (circles in figure 4), and even switch the propulsive direction (negative values of Y_x), thus equivalent to a backward net motion. Imposed oscillations are now counteracted by
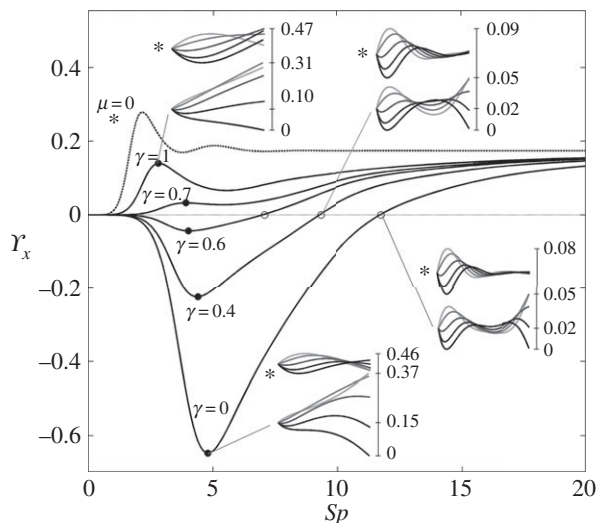
Figure 4. Scaling function Y_x, representative of the propulsive force. All cases plotted use the sliding resistance parameter value $\mu = 100$, except for the dashed line which plots the case $\mu = 0$. Waveforms corresponding to this $\mu = 0$ case are indicated by an asterisk. The local maxima/minima $Y_x(Sp_m)$ in the interval $Sp_m \in [0,5]$ are labelled by black dots. Positions of the values where $Y_x = 0$ are labelled by circles.

Figure 5. Local maxima/minima $Y_x(Sp_m)$, with $Sp_m \in [0,5]$, across the parameter space (μ, γ). The black line separates the values for which $Y_x(Sp_m)$ is negative from those for which it is positive. The region above (below) the black line indicates the positive maxima (negative minima) of $Y_x(Sp_m)$ in (μ, γ).

waves travelling in opposition at distal parts of the bundle (compare top and bottom net plots of each inset indicated by an asterisk in figure 4). Small values of γ increases the non-local counterbending amplitude and causes the propulsive force to switch direction (negative values) as Sp increases ($\gamma = 0, 0.4$ and 0.6 in figure 4). However, similarly to the Euler–Bernoulli case, increased floppiness of the filament bundle, i.e. large Sp, causes the amplitude of deformation to decay (both amplitude of imposed oscillation and counter-waves), reducing in this way the magnitude of the propulsive force which is now characterized by the appearance of a minimum value (see $\gamma = 0$ in figure 4).

The zero values of Y_x for $\gamma = 0, 0.4$ and 0.6, circles in figure 4, are therefore a genuine manifestation of the perfect hydrodynamic balance between the imposed oscillation at the proximal end and the counter-waves at the distal end, with amplitudes modulated by the effective bundle stiffness Sp. Increased bundle floppiness causes the counter-wave amplitude to vanish, thus the change in sign to positive values of the propulsive force $\bar{F}_x$ before it plateaus to a constant positive level, similarly to the Euler–Bernoulli filaments. The lower plateau value for filament bundles is due to the added effective stiffness arising from the cross-linking mechanics. The separatrix in figure 5 captures the region in parameter space where the local extrema of $Y_x(Sp_m)$ changes sign, the non-trivial roots of Y_x (circles) in figure 4. This indicates the region where a significant influence of non-local counterbend effect is predicted, and illustrates how the triad (Sp, μ, γ) may be conveniently tuned to achieve zero, forward or backward propulsion (figure 5). Reversal in swimming direction may be achieved by simply increasing the frequency of oscillation for instance, recalling that $Sp = L(\zeta_\perp \omega / E)^{1/4}$. It is worth noting that the cross-linking dissipation does not affect the main elasto-hydrodynamic characteristics, governed by the penetration length $\ell_\omega = L/Sp$ [8], as indicated by the positive asymptote for both Euler–Bernoulli filaments and filament bundles in figure 4.
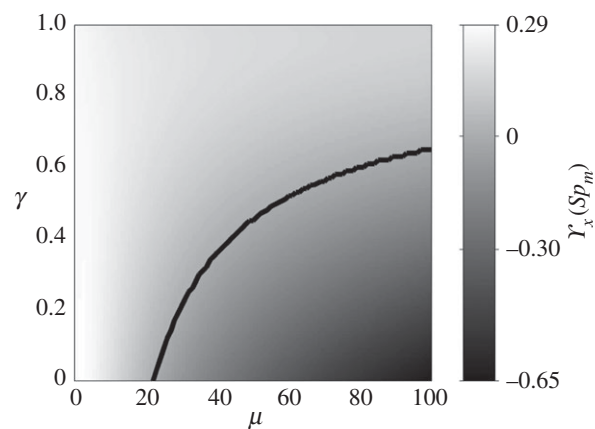
2.2. The bimodal length-dependent relaxation dynamics

The cross-linking mechanics introduces a diffusion-like time scale, $L^2 \zeta_\perp / a^2 k$, with a somewhat weaker L^2 geometrical dependence, in addition to the high-order, hyperdiffusive scaling $L^4 \zeta_\perp / E$. Indeed, the cross-linking resistance $\mu = a^2 L^2 k / E$ contrasts the elastohydrodynamic and cross-linking time scales. The cross-linking resistance depends on geometrical aspects of the bundle, as μ measures the ratio between the natural cross-linking elastic length $\ell = \sqrt{E/a^2 k}$ relative to total axial length via $\mu = (L/\ell)^2$. The cross-linking elastic length ℓ has an important biophysical interpretation: it is the dimensional length by which cross-linking effects become prevalent. The cross-linking mechanics become increasingly important when $L > \ell$, while the opposite is found for $L \sim O(\ell)$ or smaller. The latter entails the possibility of studying relaxation counterbend phenomena by only varying the length of the filament bundle, and motivates rescaling μ relative to the reference length L_0, so that $\mu(L) = L^2 \mu_0$, $\mu_0 = a^2 L_0^2 k / E$ and now $L = L/L_0$, with smallest dimensionless length $L = 1$.

The non-local, counterbend dynamics decaying from initial data, with an amplitude a_n, is depicted in figure 6 for filament bundles that are clamped at the proximal end (the electronic supplementary material, S1). This is characterized by an effective relaxation constant λ_n^{-4} via $\alpha(s, t) = \sum_n a_n S_n(s) e^{-\lambda_n^4 t}$, with $S_n = C_1 \sin(q_{1_n} s) + C_2 \cos(q_{1_n} s) + C_3 \sinh(q_{2_n} s) + C_4 \cosh(q_{2_n} s)$ for a given participating mode n. The triad of dissipative contributions acts as an effective dispersion medium for both bending and cross-linking deformations, dictated by the same dispersion relation. However, the mode shape is captured by the wavenumber–eigenvalue coupling $q_{l_n} = \sqrt{\left(\sqrt{\mu^2 + 4\lambda_n^4} + (-1)^l \mu\right)/2}$ for $l = 1, 2$, which is not only influenced by the effective relaxation constant, reminiscent of pure high-order elastohydrodynamic dissipation, but also by the cross-linking diffusion. Boundary conditions define the transcendental solvability condition for λ_n, which depend implicitly on both μ and γ, with an infinite number of mode solutions for each
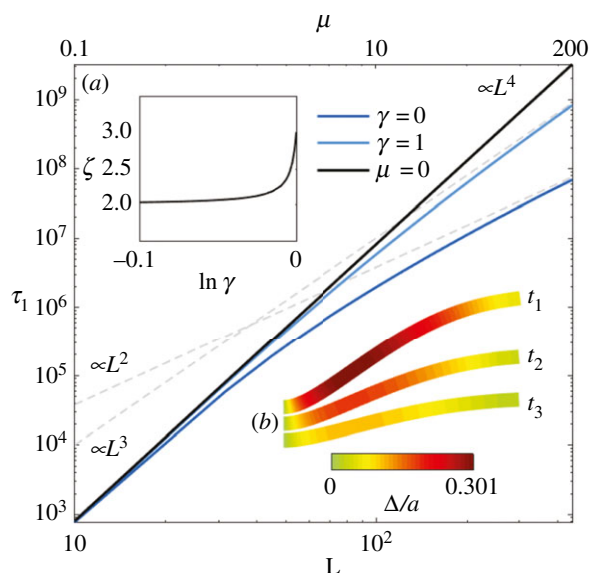
Figure 6. Rescaled relaxation time τ_1 for the first mode as a function of L for the Euler–Bernoulli filaments ($\mu = 0$, black curve) and filament bundles (blue curves). The grey dashed lines indicate the long-length asymptote L^2 and L^3 for filament bundles (labelled by '$\propto L^{3'}$ and '$\propto L^{2'}$ at the bottom left corner). The top horizontal axis shows the associated μ values via the relationship $\mu(L) = L^2 \mu_0$. The inset (a) plots the exponent ζ of the relationship $\tau_1 \propto L^\zeta$, as calculated for long filament bundles, against $\ln \gamma$; (b) shows the time evolution of the relaxation dynamics of the first mode, with the overlaid colours indicating the rescaled sliding displacement Δ/a, for the case $\mu = 100$ and $\gamma = 0$. (Online version in colour.)

parameter set. Curve-fitting expressions for λ_1 obtained from numerical solutions are presented in the electronic supplementary material, S1.

The non-local cross-linking diffusion introduces a bimodal length-dependent material response, as illustrated in figure 6 for the relaxation time of the fundamental mode

$$\tau_1(L) = \left(\frac{L}{\lambda_1(L)} \right)^4 .$$

The relaxation dynamics of Euler–Bernoulli filaments decay with a characteristic L^4-dependence associated with the filament elastohydrodynamic hyperdiffusion [8]. When $\mu = 0$, λ_1 is a constant solely defined by boundary conditions, thus $\tau_1 \propto L^4$ as discussed above. This canonical case is shown by the black straight curve in figure 6, also indicated by the '$\propto L^{4'}$ at the top right corner of figure 6. The relaxation dynamics of filament bundles, on the other hand (depicted by the light blue and dark blue curves), deviate from the canonical L^4-dependence (straight black curve) as L increases, or equivalently μ (the top horizontal axis in figure 6 shows the associated μ values via the relationship $\mu(L) = L^2 \mu_0$). This is due to the fact that, for filament bundles, $\lambda_1 = \lambda_1(L)$, thus inducing an additional length dependence on the denominator of τ_1. This causes the relaxation time to gradually deviate from the classical L^4-dependence, with greater magnitude as L increases, depending on the details of the basal compliance. For $\gamma = 0$, the deviation from the Euler–Bernoulli case starts approximately from $\mu > 1$, while, for $\gamma = 1$, it occurs for approximately $\mu > 10$. An L^2 asymptote arises for long filament bundles with $\gamma = 0$, while for $\gamma = 1$ the transition is to an L^3 behaviour instead. These long-length asymptotes are indicated by the dashed grey curves labelled by '$\propto L^{3'}$ and '$\propto L^{2'}$ at the bottom left corner of figure 6.

The length-dependent transition between L^2 and L^3 asymptotes for long filament bundles is governed by the basal compliance. This γ-dependence is depicted in the inset (a) of figure 6, which plots the exponent ζ of the relationship $\tau_1 \propto L^\zeta$ in the limit of large L. For asymptotically long filament bundles, the exponent of $\tau_1 \propto L^\zeta$ is quadratic ($\zeta = 2$), and remains nearly quadratic until γ approaches 1, at which $\zeta = 3$. Such bijection of the material response entails that simultaneous measurement of the bundle mechanical properties, in different material directions, can be extracted from simple relaxation experiments. In particular, increased inter-filament sliding, concentrated towards the clamped end, induces curvature reversal for long filament bundles (figure 6 inset (b)), reminiscent of the counterbend phenomenon [34]. Boundary conditions require zero contact forces and torques at the free end, while clamped constraint facilitates the accumulation of cross-linking sliding towards the proximal end. Both bending and cross-linking deformations relax towards the reference configuration with the same effective rate λ_1. Figure 6 inset (b) shows the simultaneous hyperdiffusive relaxation of bundle curvature (bundle shape) and sliding displacement (overlaid colour) towards the equilibrium straight configuration. Figure 6 thus summarizes the impact of the cross-linking mechanics on the relaxation time across the parameter space (γ, μ).

3. Discussion

We studied the transient and post-transient dynamics of over-damped filament bundles that are interconnected by linking elastic proteins. Deformations in distinct material directions, arising from the cross-linking interfilament sliding and pure bending deformation, are coupled with local slender-body hydrodynamics. This leads to an effective dispersion mechanism governed by the superposition of short- and long-range dissipation mechanisms. Cross-linking stresses are transmitted to distant parts of the bundle via boundary balance of moments. The cumulative moments are able to surpass the high-order elastohydrodynamic dissipation, and shape the bundle structure non-locally, with increased influence for long filament bundles, or equivalently, large μ.

The delicate interplay between the interfilament sliding at the base and the rest of the bundle results in a bimodal dynamic response, which departs from the classical Euler–Bernoulli theory [6,8,32]. When the basal sliding is permitted, cross-linking diffusion is mostly local, and acts to effectively reinforce the bundle structure. Long-range curvature-reversal events, however, are magnified when the basal sliding is constrained [34]. The counterbend dynamics generate spontaneous travelling waves in opposition to driven oscillations, which are capable of suppressing the propulsive potential, and even reverting the direction of propulsion (figure 4). Curvature perturbations diffuse more rapidly, a hundred times faster than Euler–Bernoulli hyperdiffusion with an equivalently higher bending rigidity (figure 6). Relatively small cross-linking deformations, up to only 30% of the bundle diameter, are capable of exciting large counterbend modes (figure 6 inset (b)), and induce a bimodal $L^2 - L^3$ length-dependent deviation from the L^4-dependence of canonical filaments. Paradoxical measurements may arise if standard Euler–Bernoulli theory is used to interpret experiments [29,31,33,37], as exemplified by the paradoxical

length-dependent bending stiffness in microtubules [59]. Indeed, the length deviation predicted here may be mistakenly interpreted as an effective length-dependent bending rigidity via $L^4\zeta_\perp/E(L)$ [8], if rather the Euler–Bernoulli theory is used; de facto, the Euler–Bernoulli theory is traditionally used since the first measurements of flagellar bundles [27,29,31].

Static, force-displacement experiments that are often used to probe flagellar material quantities [29,31,33,38] are cumbersome (figure 1a). They require high-precision force-calibrated probes and micro-manipulators, and often rely on the rare attachment of the filament's tip to the coverslip to microprobe actuation [29,31,33]. This proximity of the filament bundle to the coverslip can interfere with the interfilament sliding due to surface adhesion, biasing in this way force and shape measurements [34]. The counterbend dynamics provides a simpler and robust empirical route for the disentanglement of material parameters. This includes measurements of the basal interfilament elasticity, despite being deeply embedded at the connecting piece of the bundle (figure 1). As a result, standard microfluidic designs may be explored to induce shape changes dynamically [18]. Likewise, the dynamical counter-wave phenomenon may also inspire the design of artificial swimmers [60] that are able to reverse the swimming direction by simply increasing, for instance, the frequency of oscillation (figure 4).

The counter-wave phenomena becomes increasingly important for bundles longer than $\ell = \sqrt{E/a^2k}$, typically 5 μm for flagella [2,7,36,49,61,62]. Interestingly, the majority of eukaryotic flagella exceed ℓ by a few orders of magnitude, from approximately 30 μm for *Chlamydomonas* and sea urchin sperm to almost 200 μm for quail sperm [61,62]. Cross-linking effects may also become increasingly important during flagellar growth, and influencing in this way the wave coordination during flagellar reconstitution in *Chlamydomonas* [63]. Molecular motors organization thus may operate differently for $L < \ell$ and $L > \ell$. Indeed, local flagellar control models [7,49] recently gained empirical support when tested against short flagella experiments [49], a regime where counterbend phenomenon may be negligible ($L < \ell$). This is despite of the well-known negative support of curvature control models [36,41], tested instead against long flagella ($L > \ell$). The recurrent contradictions between sliding and curvature control models [7,11,36,41,49,52] may suggest the occurrence of distinct length-dependent flagellar regimes.

Linear models coupling the molecular motor reaction kinetics with interfilament sliding spontaneously propagate waves along the axoneme via a Hopf bifurcation [11,36, 42,45,48]. The resulting wave train is observed to move from tip to base, i.e. in the direction opposite to what one would expect from a local dissipation theory (when the interfilament sliding is prevented at the base) [11,49,56]. Incidentally, the basal compliance was observed to influence the direction of wave propagation in flagella self-organization models [36,56], demonstrating the sensitivity of the direction of the travelling wave to details of the connecting piece (basal part) and boundary conditions. This is in agreement with the bimodal response predicted here (figure 2), in which counterbend is maximized when $\gamma = 0$ [34]. The wave direction is influenced non-locally by cross-linking effects whose magnitude is regulated by the basal interfilament sliding (figures 2 and 6). This might explain the surprising significance of the basal compliance during the flagellar wave coordination observed recently in empirical

studies [61], and even flagellar synchronization that may arise without recurring to hydrodynamical coupling [64]. Nevertheless, the mechanisms by which the flagellar wave direction is selected is poorly understood. Previous studies were reduced to the linear level, and at the nonlinear regime, the dynamical instability generates unstable travelling waves that can propagate in both directions, with potential for multi-frequency modes [54,65]. The boundary conditions and basal mechanics assist the mode selection nonlinearly, and thus the direction of propagation, emphasizing how the flagellar dynamics is critically dependent on the underlying structural mechanics of the axoneme. Non-local hydrodynamic interactions [62], transversal axonemal deformations [44,47] and geometrical non-linearities [10,39] are also likely to affect the emergence of self-organization in flagellar systems.

The high-order diffusive interaction, intrinsic to elastohydrodynamic systems in equation (2.1), is observed throughout nature. In non-dilute systems, particles are affected by density variations beyond the nearest neighbours via, for example, biharmonic interactions $u_t = D_1\nabla^2 u - D_2\nabla^4 u$ [66,67], thus closely related to equation (2.1). Despite the relatively short-range influence, such higher-order diffusion instigates complex spatio-temporal dynamics and self-organization in all fields of science [68,69]. They drive instabilities and even mediate the coexistence of spatial patterns and temporal chaos, as observed in Kuramoto–Sivashinsky systems [69]. Other exemplars of local, higher-order diffusion are found in Ginzburg–Landau superconductors, spatial patterning in Cahn–Hilliard and biochemical systems, plus generalized Fisher–Kolmogorov models, water waves and continuum mechanics systems, among others [66,68,69].

In contrast with canonical high-order diffusion systems [66,68,69], the flagellar scaffold, or equivalently, any cross-linked filament-bundle immersed in a viscous fluid is governed by high-order dispersion medium that is inherently *non-local*. Here, the biharmonic diffusion arises instead via a *local* elastohydrodynamic dissipation [6,8], while the Fickian-like interaction arises through the *long-range* coupling reflecting the bundle mechanics [7,11,34,35], effectively connecting distant parts of the system via boundary bending moments. This unveils the potential for rich long-range phenomena via reaction–diffusion interactions [11,54,56], from non-local pattern formation to long-range synchronization of auto-oscillators, that are yet to be fully explored in the realm of mathematical biology.

We hope that these results will inspire theoreticians and experimentalists to study the dynamical effects of the counterbend phenomenon in the filament bundle as found throughout nature, including prospects for counterbend reaction–diffusion systems in flagellar dynamics, effectively bridging, non-locally, dynamical systems and PDEs.

References

1. Howards SS. 1997 Antoine van Leeuwenhoek and the discovery of sperm. *Fertil. Steril.* **67**, 16–17. (doi:10.1016/S0015-0282(97)81848-1)

2. Satir P. 1968 Studies on cilia III. Further studies on the cilium tip and a 'sliding filament' model of ciliary motility. *J. Cell Biol.* **39**, 77–94. (doi:10.1083/jcb.39.1.77)

3. Summers KE, Gibbons IR. 1971 Adenosine triphosphate-induced sliding of tubules in trypsin-treated flagella of sea-urchin sperm. *Proc. Natl Acad. Sci. USA* **68**, 3092–3096. (doi:10.1073/pnas.68.12.3092)

4. Warner FD, Satir P. 1974 The structural basis of ciliary bend formation: radial spoke positional changes accompanying microtubule sliding. *J. Cell Biol.* **63**, 35–63. (doi:10.1083/jcb.63.1.35)

5. Satir P. 1965 Studies on cilia: Ii. examination of the distal region of the ciliary shaft and the role of the filaments in motility. *J. Cell Biol.* **26**, 805–834. (doi:10.1083/jcb.26.3.805)

6. Machin KE. 1958 Wave propagation along flagella. *J. Exp. Biol.* **35**, 796–806.

7. Brokaw CJ. 1972 Flagellar movement: a sliding filament model. *Science* **178**, 455–462. (doi:10.1126/science.178.4060.455)

8. Wiggins CH, Goldstein RE. 1998 Flexive and propulsive dynamics of elastica at low reynolds number. *Phys. Rev. Lett.* **80**, 3879. (doi:10.1103/PhysRevLett.80.3879)

9. Wiggins CH, Riveline D, Ott A, Goldstein RE. 1998 Trapping and wiggling: elastohydrodynamics of driven microfilaments. *Biophys. J.* **74**, 1043–1060. (doi:10.1016/S0006-3495(98)74029-9)

10. Gadêlha H, Gaffney EA, Smith DJ, Kirkman-Brown JC. 2010 Nonlinear instability in flagellar dynamics: a novel modulation mechanism in sperm migration? *J. R. Soc. Interface* **7**, 1689–1697. (doi:10.1098/rsif.2010.0136)

11. Camalet S, Jülicher F, Prost J. 1999 Self-organized beating and swimming of internally driven filaments. *Phys. Rev. Lett.* **82**, 1590. (doi:10.1103/PhysRevLett.82.1590)

12. Bourdieu L, Duke T, Elowitz MB, Winkelmann DA, Leibler S, Libchaber A. 1995 Spiral defects in motility assays: a measure of motor protein force. *Phys. Rev. Lett.* **75**, 176–179. (doi:10.1103/PhysRevLett.75.176)

13. Goldstein RE, Langer SA. 1995 Nonlinear dynamics of stiff polymers. *Phys. Rev. Lett.* **75**, 1094–1097. (doi:10.1103/PhysRevLett.75.1094)

14. Fu HC, Wolgemuth CW, Powers TR. 2008 Beating patterns of filaments in viscoelastic fluids. *Phys. Rev. E* **78**, 041913–041925. (doi:10.1103/PhysRevE.78.041913)

15. Yu TS, Lauga E, Hosoi AE. 2006 Experimental investigations of elastic tail propulsion at low Reynolds number. *Phys. Fluids* **18**, 0917011–0917014. (doi:10.1063/1.2349585)

16. Olson SD, Lim S, Cortez R. 2013 Modeling the dynamics of an elastic rod with intrinsic curvature and twist using a regularized stokes formulation. *J. Comput. Phys.* **238**, 169–187. (doi:10.1016/j.jcp.2012.12.026)

17. Tornberg AK, Shelley MJ. 2004 Simulating the dynamics and interactions of flexible fibers in stokes flows. *J. Comput. Phys.* **196**, 8–40. (doi:10.1016/j.jcp.2003.10.017)

18. Kantsler V, Goldstein RE. 2012 Fluctuations, dynamics, and the stretch-coil transition of single actin filaments in extensional flows. *Phys. Rev. Lett.* **108**, 038103. (doi:10.1103/PhysRevLett.108.038103)

19. Sanchez T, Chen DTN, DeCamp SJ, Heymann M, Dogic Z. 2012 Spontaneous motion in hierarchically assembled active matter. *Nature* **491**, 431–434. (doi:10.1038/nature11591)

20. Heussinger C, Schüller F, Frey E. 2010 Statics and dynamics of the wormlike bundle model. *Phys. Rev. E* **81**, 021904. (doi:10.1103/PhysRevE.81.021904)

21. Claessens MMAE, Semmrich C, Ramos L, Bausch AR. 2008 Helical twist controls the thickness of f-actin bundles. *Proc. Natl Acad. Sci. USA* **105**, 8819–8822. (doi:10.1073/pnas.0711149105)

22. Claessens MMAE, Bathe M, Frey E, Bausch AR. 2006 Actin-binding proteins sensitively mediate f-actin bundle stiffness. *Nat. Mater.* **5**, 748–753. (doi:10.1038/nmat1718)

23. Fawcett DW, Bloom W, Raviola E. 1994 *A textbook of histology*. London, UK: Chapman & Hall.

24. Afzelius B. 1959 Electron microscopy of the sperm tail. *Biophys. Cytol.* **5**, 269. (doi:10.1083/jcb.5.2.269)

25. Tolomeo JA, Holley MC. 1997 Mechanics of microtubule bundles in pillar cells from the inner ear. *Biophys. J.* **73**, 2241–2247. (doi:10.1016/S0006-3495(97)78255-9)

26. Minoura I, Yagi T, Kamiya R. 1999 Direct measurement of inter-doublet elasticity in flagellar axonemes. *Cell. Struct. Funct.* **24**, 27–33. (doi:10.1247/csf.24.27)

27. Alberts B. 2002 *Molecular biology of the cell*. New York, NY: Garland Science.

28. Howard J. 2001 *Mechanics of motor proteins and the cytoskeleton*. Sunderland, MA: Sinauer Associates.

29. Lindemann CB, Rudd WG, Rikmenspoel R. 1973 The stiffness of the flagella of impaled bull sperm. *Biophys. J.* **13**, 437–448. (doi:10.1016/S0006-3495(73)85997-1)

30. Okuno M. 1980 Inhibition and relaxation of sea urchin sperm flagella by vanadate. *J. Cell Biol.* **85**, 712–725.

31. Okuno M, Hiramoto Y. 1979 Direct measurements of the stiffness of echinoderm sperm flagella. *J. Exp. Biol.* **79**, 235–243.

32. Antman SS. 2005 Nonlinear problems of elasticity. In *Applied mathematical sciences*, (eds SS Antman, L Greengard, PJ Holmes) vol. 107. Berlin, Germany: Springer.

33. Pelle DW, Brokaw CJ, Lesich KA, Lindemann CB. 2009 Mechanical properties of the passive sea urchin sperm flagellum. *Cell Motil. Cytoskeleton* **66**, 721–735. (doi:10.1002/cm.20401)

34. Gadêlha H, Gaffney EA, Goriely A. 2013 The counterbend phenomenon in flagellar axonemes and cross-linked filament bundles. *Proc. Natl Acad. Sci. USA* **110**, 12 180–12 185. (doi:10.1073/pnas.1302113110)

35. Everaers R, Bundschuh R, Kremer K. 1995 Fluctuations and stiffness of double-stranded polymers: railway-track model. *Europhy. Lett.* **29**, 263. (doi:10.1209/0295-5075/29/3/013)

36. Riedel-Kruse IH, Hilfinger A, Howard J, Jülicher F. 2007 How molecular motors shape the flagellar beat. *HFSP. J.* **1**, 192–208. (doi:10.2976/1.2773861)

37. Lindemann CB, Macauley LJ, Lesich KA. 2005 The counterbend phenomenon in dynein-disabled rat sperm flagella and what it reveals about the interdoublet elasticity. *Biophys. J.* **89**, 1165–1174. (doi:10.1529/biophysj.105.060681)

38. Xu G, Wilson KS, Okamoto RJ, Shao J-Y, Dutcher SK, Bayly PV. 2016 Flexural rigidity and shear stiffness of flagella estimated from induced bends and counterbends. *Biophys. J.* **110**, 2759–2768. (doi:10.1016/j.bpj.2016.05.017)

39. Hines M, Blum JJ. 1978 Bend propagation in flagella. I. derivation of equations of motion and their simulation. *J. Biophys.* **23**, 41–57. (doi:10.1016/S0006-3495(78)85431-9)

40. Brokaw CJ. 1975 Molecular mechanism for oscillation in flagella and muscle. *Proc. Natl Acad. Sci. USA* **72**, 3102–3106. (doi:10.1073/pnas.72.8.3102)

41. Brokaw CJ. 1985 Computer simulation of flagellar movement. VI. simple curvature-controlled models are incompletely specified. *J. Biophys.* **48**, 633–642. (doi:10.1016/S0006-3495(85)83819-4)

42. Brokaw CJ, Rintala DR. 1975 Computer simulation of flagellar movement. III. models incorporating cross-bridge kinetics. *J. Mechanochem. Cell Motil.* **3**, 77–86.

43. Machin KE. 1963 The control and synchronization of flagellar movement. *Proc. R. Soc. Lond. Ser. B* **158**, 88. (doi:10.1098/rspb.1963.0036)

44. Lindemann CB. 1994 A 'geometric clutch' hypothesis to explain oscillations of the axoneme of cilia and flagella. *J. Theor. Biol.* **168**, 175–189. (doi:10.1006/jtbi.1994.1097)

45. Hines M, Blum JJ. 1979 Bend propagation in flagella. II. Incorporation of dynein cross-bridge kinetics into the equations of motion. *Biophys. J.* **25**, 421–441. (doi:10.1016/S0006-3495(79)85313-8)

46. Rikmenspoel R. 1971 Contractile mechanisms in flagella. *Biophys. J.* **11**, 446–463. (doi:10.1016/S0006-3495(71)86227-6)

47. Bayly PV, Wilson KS. 2014 Equations of interdoublet separation during flagella motion reveal mechanisms of wave propagation and instability. *Biophys. J.* **107**, 1756–1772. (doi:10.1016/j.bpj.2014.07.064)

48. Bayly PV, Wilson KS. 2015 Analysis of unstable modes distinguishes mathematical models of flagellar motion. *J. R. Soc. Interface* **12**, 20150124. (doi:10.1098/rsif.2015.0124)

49. Sartori P, Geyer VF, Scholich A, Jülicher F, Howard J. 2016 Dynamic curvature regulation accounts for the symmetric and asymmetric beats of Chlamydomonas flagella. *Elife.* **5**, e13258. (doi:10.7554/eLife.13258)

50. Brokaw CJ. 2014 Computer simulation of flagellar movement x: doublet pair splitting and bend propagation modeled using stochastic dynein kinetics. *Cytoskeleton* **71**, 273–284. (doi:10.1002/cm.21168)

51. Lindemann CB, Lesich KA. 2010 Flagellar and ciliary beating: the proven and the possible. *J. Cell Sci.* **123**, 519–528. (doi:10.1242/jcs.051326)

52. Brokaw CJ. 2005 Computer simulation of flagellar movement IX. Oscillation and symmetry breaking in a model for short flagella and nodal cilia. *Cell Motil. Cytoskeleton* **60**, 35–47. (doi:10.1002/cm.20046)

53. Brokaw CJ, Rintala DR. 1975 Computer simulation of flagellar movement. III. models incorporating cross-bridge kinetics. *J. Mechanochem. Cell Motil.* **3**, 77–86.

54. Oriola D, Gadêlha H, Casademunt J. 2017 Nonlinear amplitude dynamics in flagellar beating. *R. Soc. open sci.* **4**, 160698. (doi:10.1098/rsos.160698)

55. Plouraboue F, IbrahimaThiam E, Delmotte B, Climent E, Collaboration PSC. 2016 Identification of internal properties of fibers and micro-swimmers. *Proc. R. Soc. A* **473**, 20160517. (doi:10.1098/rspa.2016.0517).

56. Hilfinger A, Chattopadhyay AK, Jülicher F. 2009 Nonlinear dynamics of cilia and flagella. *Phys. Rev. E* **79**, 051918–051925. (doi:10.1103/PhysRevE.79.051918)

57. Lauga E, Powers TR. 2009 The hydrodynamics of swimming microorganisms. *Rep. Prog. Phys.* **72**, 096601. (doi:10.1088/0034-4885/72/9/096601)

58. Purcell EM. 1977 Life at low Reynolds number. *Am. J. Phys.* **45**, 3. (doi:10.1119/1.10903)

59. Pampaloni F, Lattanzi G, Jonáš A, Surrey T, Frey E, Florin E-L. 2006 Thermal fluctuations of grafted microtubules provide evidence of a length-dependent persistence length. *Proc. Natl Acad. Sci. USA* **103**, 10 248–10 253. (doi:10.1073/pnas.0603931103)

60. Gadêlha H. 2013 On the optimal shape of magnetic swimmers. *Regul. Chaotic Dyn.* **18**, 75–84. (doi:10.1134/S156035471301005X)

61. Wan KY, Goldstein RE. 2016 Coordinated beating of algal flagella is mediated by basal coupling. *Proc. Natl Acad. Sci. USA* **113**, E2784–E2793. (doi:10.1073/pnas.1518527113)

62. Gaffney EA, Gadêlha H, Smith DJ, Blake JR, Kirkman-Brown JC. 2011 Mammalian sperm motility: observation and theory. *Annu. Rev. Fluid Mech.* **43**, 501–528. (doi:10.1146/annurev-fluid-121108-145442)

63. Goldstein RE, Polin M, Tuval I. 2011 Emergence of synchronized beating during the regrowth of eukaryotic flagella. *Phys. Rev. Lett.* **107**, 148103. (doi:10.1103/PhysRevLett.107.148103)

64. Quaranta G, Aubin-Tam M-E, Tam D. 2015 Hydrodynamics versus intracellular coupling in the synchronization of eukaryotic flagella. *Phys. Rev. Lett.* **115**, 238101. (doi:10.1103/PhysRevLett.115.238101)

65. Oriola D, Gadêlha H, Blanch-Mercader C, Casademunt J. 2014 Subharmonic oscillations of collective molecular motors. *Europhy. Lett.* **107**, 18002. (doi:10.1209/0295-5075/107/18002)

66. Murray JD. 2001 Mathematical biology. II. Spatial models and biomedical applications. In *Interdisciplinary applied mathematics*, vol. 18. New York, NY: Springer.

67. Cohen DS, Murray JD. 1981 A generalized diffusion model for growth and dispersal in a population. *J. Math. Biol.* **12**, 237–249. (doi:10.1007/BF00276132)

68. Peletier LA, Troy WC. 2012 *Spatial patterns: higher order models in physics and mechanics*, vol. 45. New York, NY: Springer Science & Business Media.

69. Pikovsky A, Rosenblum M, Kurths J, Hilborn RC. 2002 Synchronization: a universal concept in nonlinear science. *Am. J. Phys.* **70**, 655–655. (doi:10.1119/1.1475332)